Original Article

Prediction of early lung adenocarcinoma spread through air spaces by machine learning radiomics: a cross-center cohort study

Cong Liu[1]^, Ao Meng[2], Xiu-Qing Xue[3], Yu-Feng Wang[4], Chao Jia[5], Da-Peng Yao[6], Yun-Jian Wu[5], Qian Huang[2], Ping Gong[2], Xiao-Feng Li[5]

[1]Department of Minimally Invasive Oncology, Xuzhou New Health Geriatric Hospital, Xuzhou, China; [2]School of Medical Imaging, Xuzhou Medical University, Xuzhou, China; [3]Department of Nuclear Medicine, The First People's Hospital of Yancheng, Yancheng, China; [4]Department of Nuclear Medicine, The Xuzhou Hospital Affiliated to Jiangsu University, Xuzhou, China; [5]Department of Radiology, The Xuzhou Hospital Affiliated to Jiangsu University, Xuzhou, China; [6]Department of Radiology, Xuzhou New Health Geriatric Hospital, Xuzhou, China

Contributions: (I) Conception and design: XF Li, P Gong; (II) Administrative support: XF Li, P Gong, XQ Xue, YF Wang; (III) Provision of study materials or patients: DP Yao, XQ Xue; (IV) Collection and assembly of data: C Jia, YJ Wu; (V) Data analysis and interpretation: C Liu, A Meng, Q Huang; (VI) Manuscript writing: All authors; (VII) Final approval of manuscript: All authors.

Correspondence to: Xiao-Feng Li, MD, PhD. Department of Radiology, The Xuzhou Hospital Affiliated to Jiangsu University, No. 131 Huancheng Road, Gulou District, Xuzhou 221000, China. Email: lxf5818@163.com.

Background: Sublobar resection is suitable for peripheral stage I lung adenocarcinoma (LUAD). However, if tumor spread through air spaces (STAS) present, the lobectomy will be considered for a survival benefit. Therefore, STAS status guide peripheral stage I LUAD surgical approach. This study aimed to identify radiological features associated with STAS in peripheral stage I LUAD and to develop a predictive machine learning (ML) model using radiomics to improve surgical decision-making for thoracic surgeons.

Methods: We conducted a retrospective analysis of patients who underwent surgical treatment for lung tumors from January 2022 to December 2023, focusing on clinical peripheral stage I LUAD. High-resolution computed tomography (CT) scans were used to extract 1,581 radiomics features. Least absolute shrinkage and selection operator (LASSO) regression was applied to select the most relevant features for predicting STAS, reducing model overfitting and enhancing predictability. Ten ML algorithms were evaluated using performance metrics such as area under the receiver operating characteristic curve (AUROC), accuracy, recall, F1-score, and Matthews Correlation Coefficient (MCC) after a 10-fold cross-validation process. SHapley Additive exPlanations (SHAP) values were calculated to provide interpretability and illustrate the contribution of individual features to the model's predictions. Additionally, a user-friendly web application was developed to enable clinicians to use these predictive models in real-time for assessing the risk of STAS.

Results: The study identified significant associations between STAS and radiological features, including the longest diameter, consolidation-to-tumor ratio (CTR), and the presence of spiculation. The Random Forest (RF) model for 3-mm peritumoral extensions demonstrated strong predictive performance, with a Recall_Mean of 0.717, Accuracy_Mean of 0.891, F1-Score_Mean of 0.758, MCC_Mean of 0.708, and an AUROC_Mean of 0.944. SHAP analyses highlighted the influential radiomics features, enhancing our understanding of the model's decision-making process.

Conclusions: The RF model, employing specific intratumoral and 3-mm peritumoral radiomics features, was highly effective in predicting STAS in peripheral stage I LUAD. This model is recommended for clinical use to optimize surgical strategies for LUAD patients, supported by a real-time web application for STAS risk assessment.

^ ORCID: 0000-0002-5056-0474.

Keywords: Radiomics; machine learning (ML); lung adenocarcinoma (LUAD); tumor spread through air spaces (STAS)

Submitted Jul 02, 2024. Accepted for publication Nov 26, 2024. Published online Dec 27, 2024.
doi: 10.21037/tlcr-24-565
View this article at: https://dx.doi.org/10.21037/tlcr-24-565

Introduction

The use of low-dose computed tomography (LDCT) for screening high-risk populations has significantly improved early detection rates of lung cancer. Recent data show that 3.48% of individuals screened with LDCT are diagnosed with lung cancer, with 81.09% of these cases identified at stage I, predominantly as adenocarcinomas (1). Surgical resection is the primary treatment recommendation for these patients. Advances in surgical techniques are noteworthy. For instance, according to Suzuki's study, for early-stage lung adenocarcinoma (LUAD) with a size smaller than 2 cm and a consolidation-to-tumor ratio (CTR) less than 0.5, sublobar resection provides comparable efficacy to lobectomy (2). Altorki's study also demonstrated that in patients with peripheral non-small cell lung cancer (NSCLC) with tumor sizes of 2 cm or less and pathologically confirmed node-negative status in the hilar and mediastinal lymph nodes, sublobar resection was non-inferior to lobectomy in terms of disease-free survival (3).

The concept of tumor spread through air spaces (STAS), recognized by the World Health Organization in 2015 as a unique pattern of lung cancer metastasis, has profoundly impacted the management of stage I LUAD (4). Ren's study indicated that STAS is an independent risk factor for recurrence following sublobar resection (5). Eguchi's findings show that stage I LUAD patients with positive STAS indications benefit more from lobectomy than sublobar resection (6). This evidence suggests that the presence of STAS should contraindicate sublobar resection due to its strong association with decreased disease-free survival (hazard ratio =1.975, 95% confidence interval: 1.691–2.307), confirming its role as a prognostic indicator of poor outcomes (7,8). In addition, for early-stage lung cancer without invasive features, sublobar resection is appropriate as it preserves more lung tissue, ensuring the patient's quality of life (3). Despite pathology's pivotal role in diagnosing STAS, the lack of standardized criteria for its diagnosis via intraoperative frozen sections significantly affects surgical decision-making (9). The limited sensitivity (50%) and low negative predictive value (8%) of these sections underscore the need for more reliable diagnostic methods (10). Currently, obtaining sufficient lung tissue to diagnose STAS through non-surgical means is not feasible, emphasizing the critical role of radiological data in the diagnosis of STAS. Machine learning (ML), especially when integrated with radiomics, is emerging as a key tool in clinical research. Our previous network meta-analysis suggested that ML models using peritumoral radiomics signatures hold considerable promise in predicting STAS (11). This study aims to identify radiological features associated with STAS in peripheral stage I lung

Highlight box

Key findings

- In peripheral stage I lung adenocarcinoma (LUAD), preoperative radiological features of the lesions-longest diameter, consolidation-to-tumor ratio, spiculation, internal vascular sign, and bronchial anomaly sign-are independent risk factors for the development of tumor spread through air spaces (STAS).
- The Random Forest (RF) model based on radiomics features of intratumoral and 3-mm peritumoral areas outperforms other machine learning models in predicting STAS of peripheral stage I LUAD.

What is known and what is new?

- For peripheral stage I LUAD without STAS, sublobar resection is appropriate. But diagnose STAS via intraoperative frozen sections has limited sensitivity (50%) and low negative predictive value (8%).
- The RF model, employing specific intratumoral and 3-mm peritumoral radiomics features, was highly effective in predicting STAS in peripheral stage I LUAD.

What is the implication, and what should change now?

- The model is recommended for clinical use to optimize surgical strategies for LUAD patients, supported by a real-time web application for STAS risk assessment.
- We should pay more attention to the important role of STAS in the diagnosis and treatment of peripheral stage I LUAD, especially for patients with peripheral stage I LUAD who need to take a sublobar resection approach as well as the status quo such as the unsatisfactory diagnostic efficacy of STAS in intraoperative frozen sections.

neoplasms and to develop a predictive ML model based on preoperative radiomics signatures of patients with peripheral stage I LUAD. The goal is to enhance STAS assessments in this patient cohort, thereby assisting thoracic surgeons in selecting the optimal surgical approach. This strategy aims to improve surgical planning and patient outcomes through imaging analyses and sophisticated ML techniques. We present this article in accordance with the STARD (12) and CLEAR reporting checklists (13) (available at https://tlcr.amegroups.com/article/view/10.21037/tlcr-24-565/rc).

Methods

Patients and clinical data

This retrospective analysis utilized data collected from January 2022 to December 2023. We obtained clinical and radiological data from patients who underwent surgical treatment for lung tumors at the Xuzhou Hospital Affiliated to Jiangsu University, supplemented with an external validation set from another hospital. The inclusion criteria were: (I) clinical stage T1–T2aN0M0, according to the 8th edition of the American Joint Committee on Cancer (AJCC) cancer staging manual (14); (II) tumors located in the outer two-thirds of the lung field on chest computed tomography (CT) axial images, with the tumor center within this specified area; (III) radical resection for lung cancer and systematic lymph node dissection with at least 6 lymph nodes excised (15); (IV) postoperative pathological diagnosis confirmed as adenocarcinoma. Exclusion criteria were: (I) multiple pulmonary neoplastic lesions diagnosed preoperatively or synchronous primary or multiple primary lung cancers (≥2 lesions) identified postoperatively; (II) preoperative exposure to radiotherapy, chemotherapy, immunotherapy, or targeted therapy for cancer; (III) a history of other malignant tumors within the past three years. STAS is defined as micropapillary, solid and/or single tumor cell clusters beyond the edge of the main mass and distinct from processing artifacts (16). The diagnosis of STAS at both Center 1 and Center 2 was performed by senior pathologists in each center based on identical diagnostic standards, ensuring a consistent evaluation across the study. Additionally, another senior pathologist at Center 1 conducted a retrospective review of the STAS diagnoses for all pathologies included in the study, and any discrepancies were re-evaluated to reach a final determination.

The study was conducted in accordance with the Declaration of Helsinki (as revised in 2013). The study was approved by The Xuzhou Hospital Affiliated to Jiangsu University Institutional Review Board (No. 2023-02-027-K01). Written informed consent was exempted due to the retrospective nature.

Image acquisition

All CT scans were performed using GE Discovery 750HD, SIEMENS SOMATOM Definition AS, and SOMATOM Definition Flash scanners (Siemens Healthineers, Erlangen, Germany), spanning from the apex to the base of the lungs. Patients were positioned supine, with scan parameters set at a tube voltage of 120 kV and an automatic tube current ranging from 80 to 350 mA. The rotation time was 0.5–0.6 seconds per rotation. The standard scanning slice thickness and interval were 5 mm, with a reconstructed slice thickness and interval of 0.6–0.625 mm, and a display field of view (DFOV) of 40 cm × 45 cm. Images were analyzed using both lung (window width 1,500 HU, window level –450 HU) and mediastinal (window width 350 HU, window level 35 HU) settings. For contrast-enhanced scans, iodinated contrast agent iohexol (350 mg/mL) was administered intravenously at a rate of 3 mL/s, with a dosage of 1.5–2.0 mL/kg. Arterial and venous phase scans were conducted 10 and 30 seconds, respectively, after the aortic threshold reached 80 HU.

Image evaluation and data measurement

Two thoracic radiology specialists, C.J. with 11 years of experience and X.F.L. with 5 years, performed detailed tumor measurements on 1-mm thick axial CT lung window images. A senior radiologist verified the accuracy of these measurements, and the average of two measurements was taken. The assessment included the longest diameter, size of solid components, lymph node short diameter, and CTR. Pure ground glass nodules, solid nodules, and part-solid nodules were categorized with CTRs of 0, 1, and 0 to 1, respectively.

Radiomics feature extraction/selection

Image preprocessing and lesion expansion

A radiologist independently performed tumor segmentation using 3D Slicer software (version 5.3.0-2023-08-03 r31920/7ef5961). DICOM images were imported from

the Picture Archiving and Communication System (PACS) and processed with tools such as "Grow from Seeds" for lesion region of interest (ROI) generation and "Erase" for precise adjustments. Finalized ROIs were saved in .nii format. To ensure consistency in spatial resolution, all images were resampled to a uniform pixel spacing of 1 mm × 1 mm × 1 mm using the SimpleITK toolkit, and Z-score normalization was applied to minimize equipment variability (17). For invasive analysis, each tumor ROI underwent expansion processes of 3 mm and 5 mm, defining focal areas for further study.

Feature extraction

The Pyradiomics toolkit successfully extracted 1,581 radiomics features from both original and processed images. These features include transformations such as wavelet, exponential, gradient, and Gaussian Laplacian, integral for enhanced model analysis. The features breakdown includes 306 histogram features, 408 Gray-Level Co-occurrence Matrix (GLCM) features, 272 Gray-Level Run-length Matrix (GLRLM) features, 272 Gray-Level Size Zone Matrix (GLSZM) features, 85 Neighborhood Gray-Tone Difference Matrix (NGTDM) features, and 238 Gray Level Dependence Matrix (GLDM) features. A heatmap with the distribution of all features is available in the Figure S1.

Feature selection and analysis

Conventional radiological features and semantics

This category included conventional radiological features such as the longest diameter, size of solid components, lymph node short diameter, and CTR. Initial screening utilized univariate logistic regression, followed by multivariate logistic regression to isolate features with independent predictive power. Conventional radiological features demonstrating a significance level of $P<0.1$ in the univariate analysis were further subjected to multivariate bidirectional stepwise logistic regression to establish independent predictive factors associated with STAS.

Radiomics features

Radiomics features were refined through the application of the least absolute shrinkage and selection operator (LASSO) regression model. This approach prevented overfitting and ensured that only the most predictive variables were retained. Subsequent analyses, including principal component analysis (PCA) and unsupervised clustering, validated and confirmed the predictive capacity of these refined features. PCA visualized the main sources of variance in the data, determining which features contribute most to the model's explanatory power. Unsupervised clustering explored potential patterns or groups within the data, assessing how the selected features performed in an unlabeled dataset, thus validating the consistency and differences between groups to ensure high predictive value.

Model ensemble and construction

After refining the features, a composite feature set integrating both conventional radiological and radiomic features was developed to construct predictive models. Based on the STAS status, this composite feature set was divided into a training set and a testing set using a 7:3 ratio. Within the training set, an ensemble of ten ML algorithms was employed, including Support Vector Machines (SVM), Categorical Boosting (CatBoost), Random Forest (RF), Light Gradient Boosting Machine (LGBM), eXtreme Gradient Boosting (XGB), Gradient Boosting Decision Tree (GBDT), Decision Tree, Adaptive Boosting (AdaBoost), Logistic Regression, and Naive Bayes (NB), incorporating a 10-fold cross-validation method. Model performance was evaluated based on metrics such as area under the receiver operating characteristic curve (AUROC), recall, accuracy, F1-score, and Matthews Correlation Coefficient (MCC).

Screening the best ML model

The ML algorithms that performed the best in the three modules of intratumoral, 3-mm peritumoral extension, and 5-mm peritumoral extension were identified. Models were constructed using the train set, while the stability of these models was evaluated on the test set. An external validation set verified the generalization ability of the models. The efficacy and generalization capability of the predictive models were assessed by plotting the receiver operating characteristic (ROC) curves, calibration curves, and the decision curve analyses (DCA). The predictive power and model stability across the three modules were compared by calculating the AUROC, recall, accuracy, F1-score, and MCC, thereby establishing the optimal ML model for predicting STAS.

Model interpretability analysis and application development

SHapley Additive exPlanations (SHAP) analysis clarified

the contribution of each feature to the model predictions, increasing transparency and enhancing clinical trust. A web application was developed using the R Shiny package to facilitate this process. This application allows users to input conventional radiological and radiomic features and receive predictions of STAS likelihood, streamlining clinical decision-making.

Statistical analysis

Statistical analyses were performed using SPSS software (version 26.0), R program software (version 4.3.3), and Python software (version 3.12). Depending on the distribution of the values, all results were presented as the median (first quartile, third quartile). Continuous data were analyzed using the Mann-Whitney *U* test, while categorical data were assessed using the Chi-squared test. Both continuous and categorical data were analyzed appropriately, with significance set at a P value of less than 0.05.

Results

The detailed research process of this study can be found in *Figure 1*.

Baseline characteristics

A total of 290 cases met the inclusion and exclusion criteria, with 65 cases (22.41%) testing positive for STAS. The cohort included 45.52% males and 54.48% females, with an average age of 62.00 years. Apart from diabetes (P=0.048), there were no statistically significant differences in clinical and pathological variables between Center 1 and Center 2, as all P values were greater than 0.05. Clinical and pathological variables were stratified based on STAS positivity, and univariate analysis was conducted to identify disparities, detailed in *Table 1*.

Relationship between conventional radiological features and STAS

Univariate and multivariate analyses assessed general, radiological, and semantic features of the lesions. The univariate analysis identified several statistically significant variables: pulmonary nodule type, longest diameter, size of solid components, CTR, spiculation, pleural indentation, internal vascular sign, bronchial anomaly sign, history of pulmonary disease, CAD, CEA, lymph node short diameter and lymph node metastasis, as presented in *Table 2*. Variables with P values <0.1 were further examined in a bidirectional stepwise multivariate analysis. This analysis confirmed that the longest diameter, CTR, spiculation, internal vascular sign, and bronchial anomaly sign were statistically significant (P values 0.002, <0.001, 0.004, <0.001, <0.001 respectively, see *Table 3*). Pulmonary nodule type and size of solid components were excluded from the multivariate analysis due to collinearity with CTR. The final model identified these factors as independent risk indicators for STAS occurrence in stage I lung cancer, detailed in *Table 3*.

Radiomics feature selection

The LASSO regression method reduced the initial pool of 1,581 radiomics features to key subsets for each module: 20 key features for the intratumoral module, 16 for the 3-mm peritumoral extension, and 13 for the 5-mm peritumoral extension. The detailed LASSO regression results were presented in *Figure 2*. The LASSO regression curves (*Figure 2A*,*2D*,*2G*) and cross-validation curves (*Figure 2B*,*2E*,*2H*) illustrate the selection process of features with non-zero coefficients at the optimal lambda value. Heatmaps (*Figure 2C*,*2F*,*2I*) display distinct expression patterns of these features in STAS-positive and STAS-negative samples across the three modules. PCA was employed on these features to visualize major sources of variance and evaluate feature performance (*Figure 3*), as shown in PCA scatter plots (*Figure 3A*,*3C*,*3E*) and unsupervised consensus matrix heatmaps (*Figure 3B*,*3D*,*3F*), indicating clear clustering patterns between the groups.

Integration of conventional and radiomics features for model construction

Conventional radiological features identified through bidirectional multivariate logistic regression were combined with selected radiomic features via LASSO analysis. The dataset was partitioned into a train set and a test set with a 7:3 ratio. To evaluate the features extracted from intratumoral and peritumoral areas (at 3-mm and 5-mm distances), 10 distinct ML models were applied to the training data. ROC curves were generated for these models, and performance metrics including recall, accuracy, F1-score, MCC, and AUROC were computed to facilitate a comparative analysis of model efficacy.

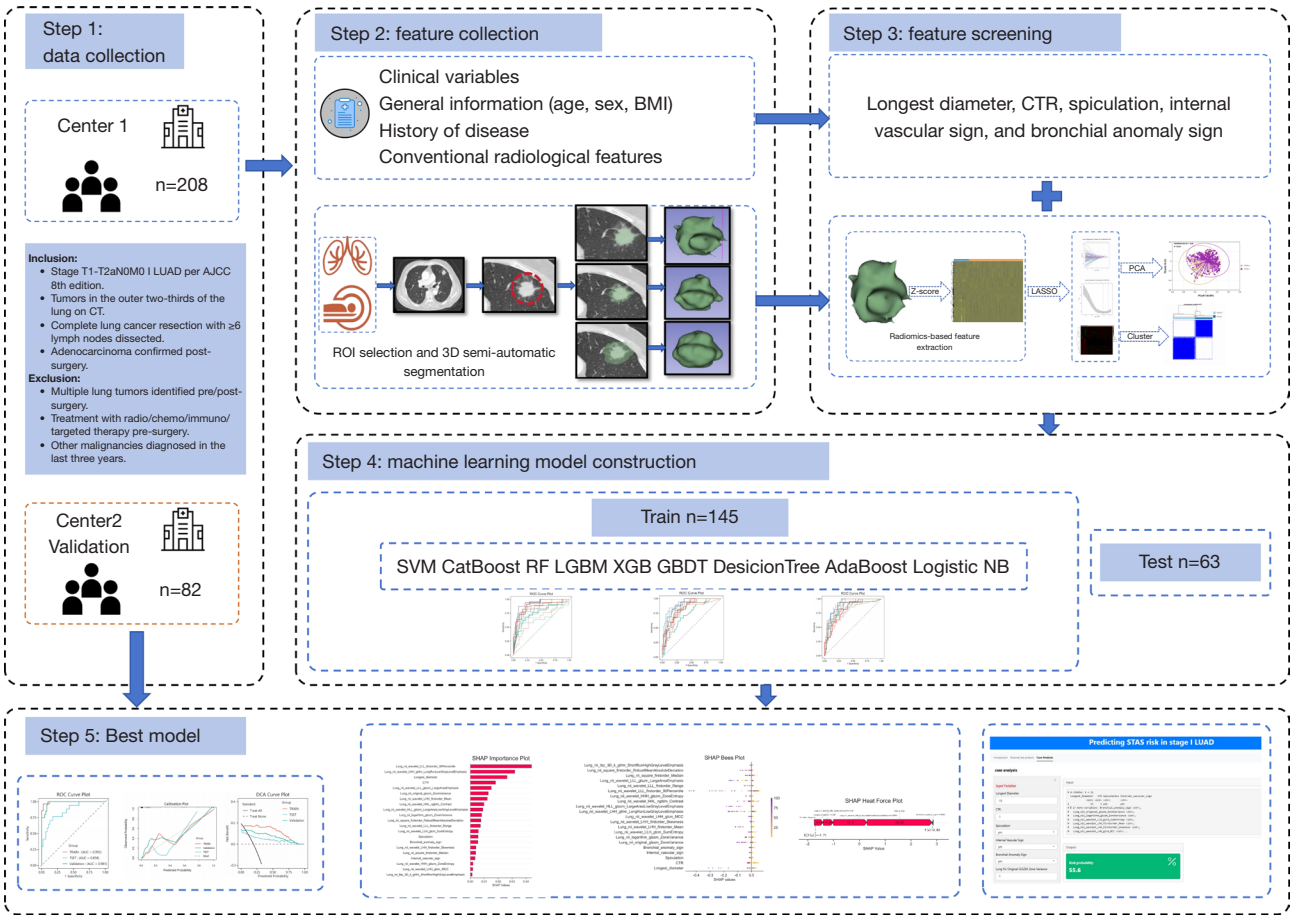

Figure 1 Workflow diagram. AUC, area under curve; CT, computed tomography; STAS, spread through air spaces; BMI, body mass index; CTR, consolidation-to-tumor ratio; SVM, Support Vector Machines; CatBoost, Categorical Boosting; RF, Random Forest; LGBM, Light Gradient Boosting Machine; XGB, eXtreme Gradient Boosting; GBDT, Gradient Boosting Decision Tree; AdaBoost, Adaptive Boosting; NB, Naive Bayes; AJCC, American Joint Committee on Cancer; ROI, Region of Interest; PCA, principal component analysis; LASSO, least absolute shrinkage and selection operator; ROC, receiver operating characteristic; DCA, decision curve analyses; SHAP, SHapley Additive exPlanations; LUAD, lung adenocarcinoma.

Performance of the selected models

The findings, detailed in *Table 4*, originate from a 10-fold cross-validation process within the train set. Logistic regression emerged as the most effective model for intratumoral analysis, yielding average performance metrics as follows: Recall_Mean of 0.584, Accuracy_Mean of 0.825, F1-Score_Mean of 0.545, MCC_Mean of 0.452, and AUROC_Mean of 0.724. For the peritumoral extensions, RF demonstrated superior performance. For the 3-mm extension, it achieved a Recall_Mean of 0.534, Accuracy_Mean of 0.833, F1-Score_Mean of 0.600, MCC_Mean of 0.455, and AUROC_Mean of 0.722. Similarly, for the 5-mm extension, it recorded a Recall_Mean of 0.483, Accuracy_Mean of 0.837, F1-Score_Mean of 0.589, MCC_Mean of 0.510, and AUROC_Mean of 0.731. Additional details on model performance can be found in Figures S2-S4 under the ROC curve analysis for each model.

Model validation and analysis

The logistic regression model for intratumoral predictions and the RF model for peritumoral extensions (at 3-mm and 5-mm) displayed superior performance in several analytical frameworks (*Figure 4*). Their efficacy was validated through ROC curve analyses (*Figure 4A*,*4D*,*4G*), decision curve analyses (*Figure 4B*,*4E*,*4H*), and calibration plots

Table 1 The comparative analysis of clinical and conventional radiological features between patients from two centers

Variables	Total (n=290)	Center 1 (n=208)	Center 2 (n=82)	Z/χ^2	P
STAS (positive)	65 (22.41)	45 (21.63)	20 (24.39)	0.26	0.61
Sex (male)	132 (45.52)	99 (47.60)	33 (40.24)	1.28	0.26
Age, years	62.00 (54.00, 68.00)	61.50 (54.00, 68.00)	62.00 (56.25, 68.00)	−0.5	0.64
BMI, kg/m^2	23.74 (21.45, 25.80)	23.74 (21.43, 25.71)	23.77 (21.45, 25.92)	−0.2	0.84
Smoking status (ever)	64 (22.07)	52 (25.00)	12 (14.63)	3.67	0.06
Location (right lung)	165 (56.90)	122 (58.65)	43 (52.44)	0.93	0.34
Lobar lung (superior lobe)	167 (57.59)	121 (58.17)	46 (56.10)	0.1	0.75
Longest diameter, cm	17.10 (11.60, 23.40)	16.50 (11.70, 22.26)	19.20 (11.53, 24.25)	−1.5	0.13
Size of solid components, cm	10.80 (0.00, 20.38)	10.05 (0.00, 19.45)	12.10 (0.00, 22.75)	−1	0.34
CTR	0.81 (0.00, 1.00)	0.67 (0.00, 1.00)	1.00 (0.00, 1.00)	−1	0.3
Lymph node short diameter, cm	6.30 (5.30, 7.50)	6.30 (5.30, 7.50)	6.40 (5.40, 7.65)	−0.6	0.52
CEA, ng/mL	2.27 (1.25, 3.90)	2.16 (1.20, 3.76)	2.48 (1.43, 4.21)	−1.1	0.26
Hypertension (positive)	68 (23.45)	48 (23.08)	20 (24.39)	0.06	0.81
Diabetes (positive)	44 (15.17)	37 (17.79)	7 (8.54)	3.91	0.05
CAD (positive)	112 (38.62)	87 (41.83)	25 (30.49)	3.19	0.07
History of pulmonary disease (positive)	169 (58.48)	120 (57.97)	49 (59.76)	0.08	0.78
Pulmonary nodule type (solid nodule)	143 (49.31)	98 (47.12)	45 (54.88)	1.42	0.23
Lobulation (positive)	206 (71.03)	150 (72.12)	56 (68.29)	0.42	0.52
Spiculation (positive)	112 (38.62)	78 (37.50)	34 (41.46)	0.39	0.53
Vacuole (positive)	68 (23.45)	43 (20.67)	25 (30.49)	3.16	0.08
Pleural indentation (positive)	122 (42.07)	92 (44.23)	30 (36.59)	1.41	0.24
Internal vascular sign (positive)	201 (69.31)	148 (71.15)	53 (64.63)	1.18	0.28
Bronchial anomaly sign (positive)	161 (55.52)	119 (57.21)	42 (51.22)	0.86	0.36

Data are expressed as median (first quartile, third quartile) or number (percentage). STAS, spread through air spaces; BMI, body mass index; CTR, consolidation-to-tumor ratio; CEA, carcinoembryonic antigen; CAD, coronary artery disease.

(*Figure 4C*,*4F*,*4I*) across train, test, and validation datasets. These models achieved impressive area under the curve (AUC) scores, indicative of their excellent predictive capabilities. The decision curve analyses underscored the clinical utility of the models by illustrating benefits across a range of decision thresholds, while the calibration plots confirmed the accuracy of the predicted probabilities in mirroring actual outcomes, thereby reinforcing the models' reliability. *Figure 5* presents a detailed evaluation of the optimal models for the intratumoral and peritumoral regions (at 3-mm and 5-mm), highlighting their notable predictive efficacy and stability, the detailed data was listed in Table S1.

SHAP value analysis and online prediction tool

We further elucidated the operation of the RF model, based on the 3-mm peritumoral radiomics features, using SHAP analysis. This analysis enhanced the interpretability of the ML model by clarifying the influence of individual features on the predictive outcomes. The SHAP importance plot (*Figure 6A*) highlighted the most influential features (top 5: Lung_nii_wavelet_LLL_firstorder_90Percentile, Lung_ni_wavelet LHH_glrim_LongRunLowGrayLevelEmphasi, Longest_diameter, CTR, Lung_ni_wavelet LLL_gIszm_LargeAreaEmphasis), and the SHAP bees plot (*Figure 6B*) provided an intricate view of the feature distribution across

Table 2 Univariate logistic regression analysis of clinical and conventional radiological features with spread through air spaces

Variables	STAS negative (n=225)	STAS positive (n=65)	Statistic	P
Sex (male)	105 (46.67)	27 (41.54)	0.53	0.47
Age, years	62.00 (53.00, 68.00)	62.00 (57.00, 69.00)	−0.86	0.39
BMI, kg/m^2	23.67 (21.36, 25.69)	23.88 (21.76, 26.12)	−0.49	0.63
Smoking status (ever)	47 (20.89)	17 (26.15)	0.81	0.37
Location (right lung)	132 (58.67)	33 (50.77)	1.28	0.26
Lobar lung (superior lobe)	132 (58.67)	35 (53.85)	0.48	0.49
Longest diameter, cm	15.80 (10.90, 21.40)	21.95 (17.25, 26.95)	−4.83	<0.001
Size of solid components, cm	5.80 (0.00, 17.60)	21.00 (10.80, 26.90)	−7.1	<0.001
CTR	0.45 (0.00, 1.00)	1.00 (1.00, 1.00)	−6.44	<0.001
Hypertension (positive)	53 (23.56)	15 (23.08)	0.01	0.94
Diabetes (positive)	38 (16.89)	6 (9.23)	2.3	0.13
CAD (positive)	97 (43.11)	15 (23.08)	8.54	0.003
History of pulmonary disease (positive)	123 (54.67)	46 (70.77)	6.08	0.01
Pulmonary nodule type (solid nodule)	89 (39.56)	54 (83.08)	38.22	<0.001
Lobulation (positive)	154 (68.44)	52 (80.00)	3.27	0.07
Spiculation (positive)	68 (30.22)	44 (67.69)	29.87	<0.001
Vacuole (positive)	58 (25.78)	10 (15.38)	3.03	0.08
Pleural indentation (positive)	85 (37.78)	37 (56.92)	7.58	0.01
Internal vascular sign (positive)	164 (72.89)	37 (56.92)	6.04	0.01
Bronchial anomaly sign (positive)	112 (49.78)	49 (75.38)	13.39	<0.001
CEA, ng/mL	2.14 (1.16, 3.31)	3.12 (1.95, 7.42)	−3.2	0.001
Lymph node short diameter, cm	6.20 (5.30, 7.40)	6.70 (5.60, 8.40)	−2.5	0.01
Lymph node metastasis (positive)	13 (5.78)	29 (44.62)	61.42	<0.001

Data are expressed as median (first quartile and third quartile) or number (percentage). STAS, spread through air spaces; BMI, body mass index; CTR, consolidation-to-tumor ratio; CAD, coronary artery disease; CEA, carcinoembryonic antigen.

the dataset. The detailed features were shown in Table S2. Additionally, the Heat Force plot (*Figure 6C*) detailed the contributions of specific features to individual predictive outcomes, offering insights into the decision-making process of the model.

To translate these analytical insights into clinical practice, an online web application was developed (https://liucong1994.shinyapps.io/app_final/). This tool enables clinicians to receive immediate predictions on the risk of STAS, facilitating enhanced decision-making. The application supports real-time data processing and features a user-friendly interface, aiming to increase the precision and efficiency of medical services. In the supplementary data (available at https://cdn.amegroups.cn/static/public/tlcr-24-565-1.xlsx), we have provided a sample file (test_data.csv) applicable to the web application. This file contains the necessary features and their values required by the model.

Discussion

This study identifies that, in addition to longest diameter and CTR, spiculation, internal vascular sign, and bronchial anomaly sign are independent risk factors for STAS in peripheral stage I LUAD, as observed on preoperative CT images. Furthermore, ML models incorporating both intratumoral and peritumoral data outperform those

Table 3 Univariate and multivariate logistic regression analysis of conventional radiological features and spread through air spaces

Variables	Univariate			Multivariate		
	Z	P	OR (95% CI)	Z	P	OR (95% CI)
Sex (male)	0.73	0.47	1.23 (0.70–2.15)	–	–	–
Age, years	1.37	0.17	1.02 (0.99–1.05)	–	–	–
BMI, kg/m^2	0.21	0.83	1.01 (0.92–1.10)	–	–	–
Smoking status (positive)	0.9	0.37	1.34 (0.71–2.54)	–	–	–
Location (right lung)	–1.1	0.26	0.73 (0.42–1.26)	–	–	–
Lobar lung (middle/lower lung)	0.69	0.49	1.22 (0.70–2.12)	–	–	–
Pulmonary nodule type (solid nodule)	5.63	<0.001	7.50 (3.72–15.13)	–	–	–
Longest diameter, cm	4.86	<0.001	1.10 (1.06–1.14)	3.09	0.002	1.07 (1.02–1.11)
Size of solid components, cm	6.23	<0.001	1.10 (1.07–1.13)	–	–	–
CTR	5.49	<0.001	13.44 (5.32–33.98)	3.98	<0.001	10.42 (3.29–33.03)
Lobulation (positive)	1.79	0.07	1.84 (0.94–3.60)	–1.7	0.09	0.44 (0.17–1.12)
Spiculation (positive)	5.21	<0.001	4.84 (2.67–8.75)	2.89	0.004	3.14 (1.45–6.82)
Vacuole (positive)	–1.7	0.09	0.52 (0.25–1.09)	–1.5	0.15	0.50 (0.19–1.28)
Pleural indentation (positive)	2.72	0.01	2.18 (1.24–3.81)	–	–	–
Internal vascular sign (positive)	–2.4	0.02	0.49 (0.28–0.87)	–4	<0.001	0.15 (0.06–0.37)
Bronchial anomaly sign (positive)	3.56	<0.001	3.09 (1.66–5.75)	4.89	<0.001	11.84 (4.39–31.91)

BMI, body mass index; CTR, consolidation-to-tumor ratio; OR, odds ratio; CI, confidence interval.

using only intratumoral data. Notably, the RF model, which includes data from both intratumoral and 3-mm peritumoral areas, demonstrates superior performance in predicting STAS in peripheral stage I LUAD compared to other ML algorithms.

For thoracic surgeons, predicting the risk of STAS from preoperative CT images in patients with peripheral stage I lung cancer is crucial for selecting the appropriate surgical approach. Additionally, Travis's study reported that after adjusting for confounding factors, including surgical approach, patients with STAS-positive stage I NSCLC still had poorer prognoses. This indicates that STAS is an aggressive feature of lung cancer (18). Eguchi (6) also noted that sublobar resection often resulted in a higher rate of local recurrence and lung cancer-specific mortality compared to lobectomy in STAS-positive stage I lung cancers, indicating that sublobar resection may not be the best option for these patients. Thus, assessing the risk of STAS using preoperative CT images is critical for choosing the surgical method.

Our study corroborates findings by Qin (19) and Toyokawa (20), identifying spiculation, internal vascular sign, and bronchial anomaly sign as independent risk factors for STAS in peripheral stage I lung cancer. These signs typically indicate a higher malignancy grade, and more malignant lesions, thus carrying a greater risk of STAS. Recent emphasis has been placed on using the size of the solid component and CTR to assess the aggressiveness of stage I lung cancer. The 8th edition of the AJCC staging for NSCLC recognizes the maximum diameter of the solid component as a critical criterion, underscoring the importance of tumor solid size in staging. Our previous research (21) confirmed a positive linear correlation between CTR and STAS occurrence in peripheral stage I LUAD, with each 0.1 increase in the ratio of the largest diameter of the tumor's solid component to the lesion's largest diameter increasing the risk of STAS by 24%. Toyokawa (20) further highlighted the value of CTR and the size of the solid component in assessing early lung cancer STAS.

Regarding ML prediction of STAS, Onozato (22) demonstrated an AUC of 0.77 in predicting STAS in peripheral stage T1aN0M0 lung cancer patients, confirming

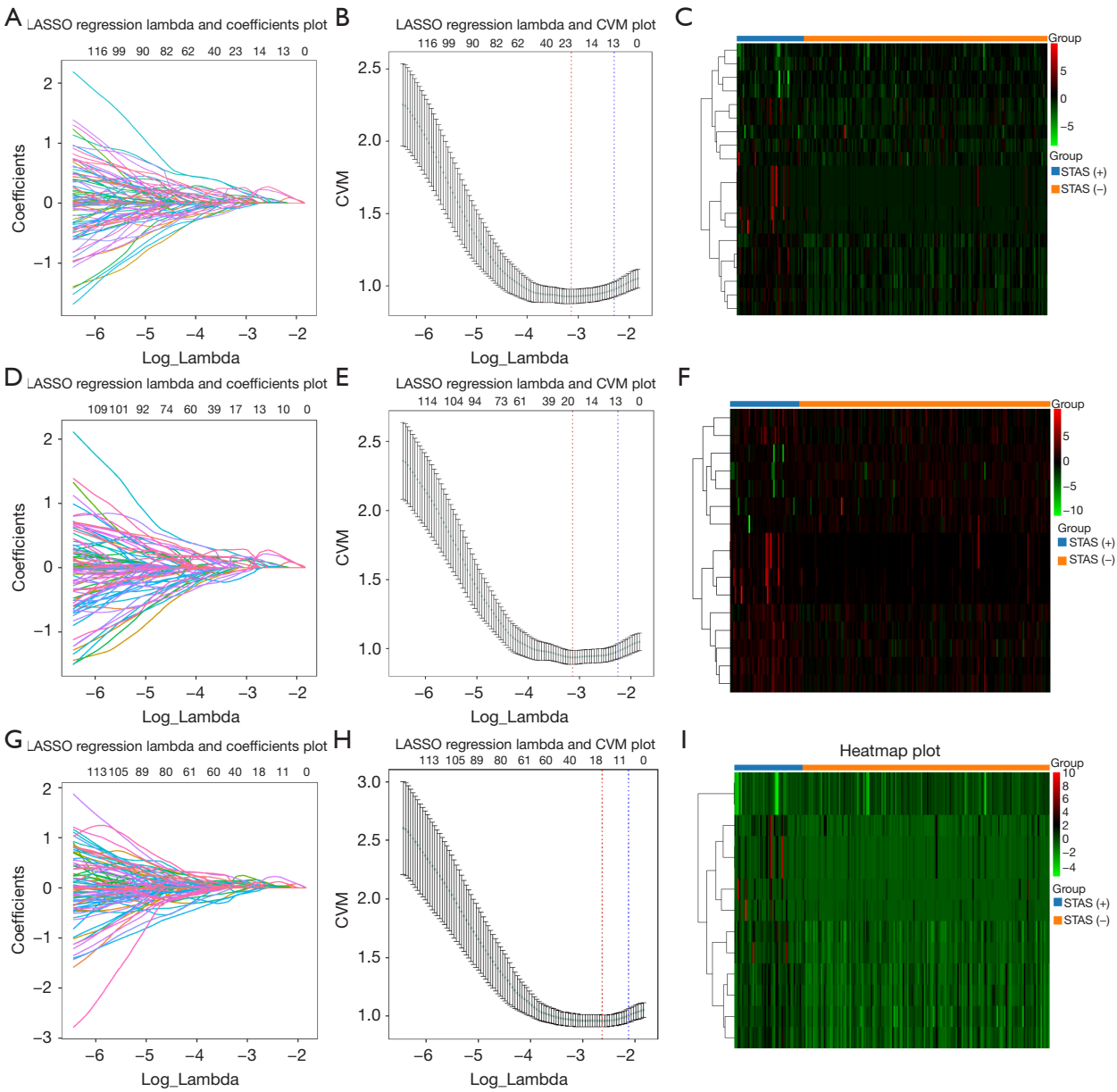

Figure 2 LASSO regression analysis of radiomics features selection within the intratumoral, and at 3-mm and 5-mm peritumoral expansions. (A) LASSO regression lambda and coefficients plot for intratumoral features, depicting the trajectory of each feature's coefficient against the log-lambda value, showcasing the feature selection process. (B) LASSO regression lambda and CVM plot for intratumoral features, indicating the lambda value with minimum error and the one standard error of the minimum (1-SE). (C) Heatmap of intratumoral features post-lasso, with hierarchical clustering dendrogram on the side, indicating groupings based on feature expression patterns. (D) LASSO regression lambda and coefficients plot for features within a 3-mm peritumoral expansion, showing how feature coefficients evolve as the regularization penalty increases. (E) LASSO regression lambda and CVM plot for the 3-mm peritumoral expansion, with marked optimal lambda values for model complexity and cross-validation error. (F) Heatmap for 3-mm peritumoral expansion features, with a dendrogram that categorizes features into clusters based on their similarity. (G) LASSO regression lambda and coefficients plot for features within a 5-mm peritumoral expansion, illustrating the selection process of features and the shrinkage effect of the lasso penalty. (H) LASSO regression lambda and CVM plot for the 5-mm peritumoral expansion, highlighting the selection of lambda for the lowest cross-validation error. (I) Heatmap of features for a 5-mm peritumoral expansion, with a dendrogram that classifies the features into distinct clusters according to their expression. LASSO, least absolute shrinkage and selection operator; CVM, cross-validation mean; STAS, tumor spread through air spaces.

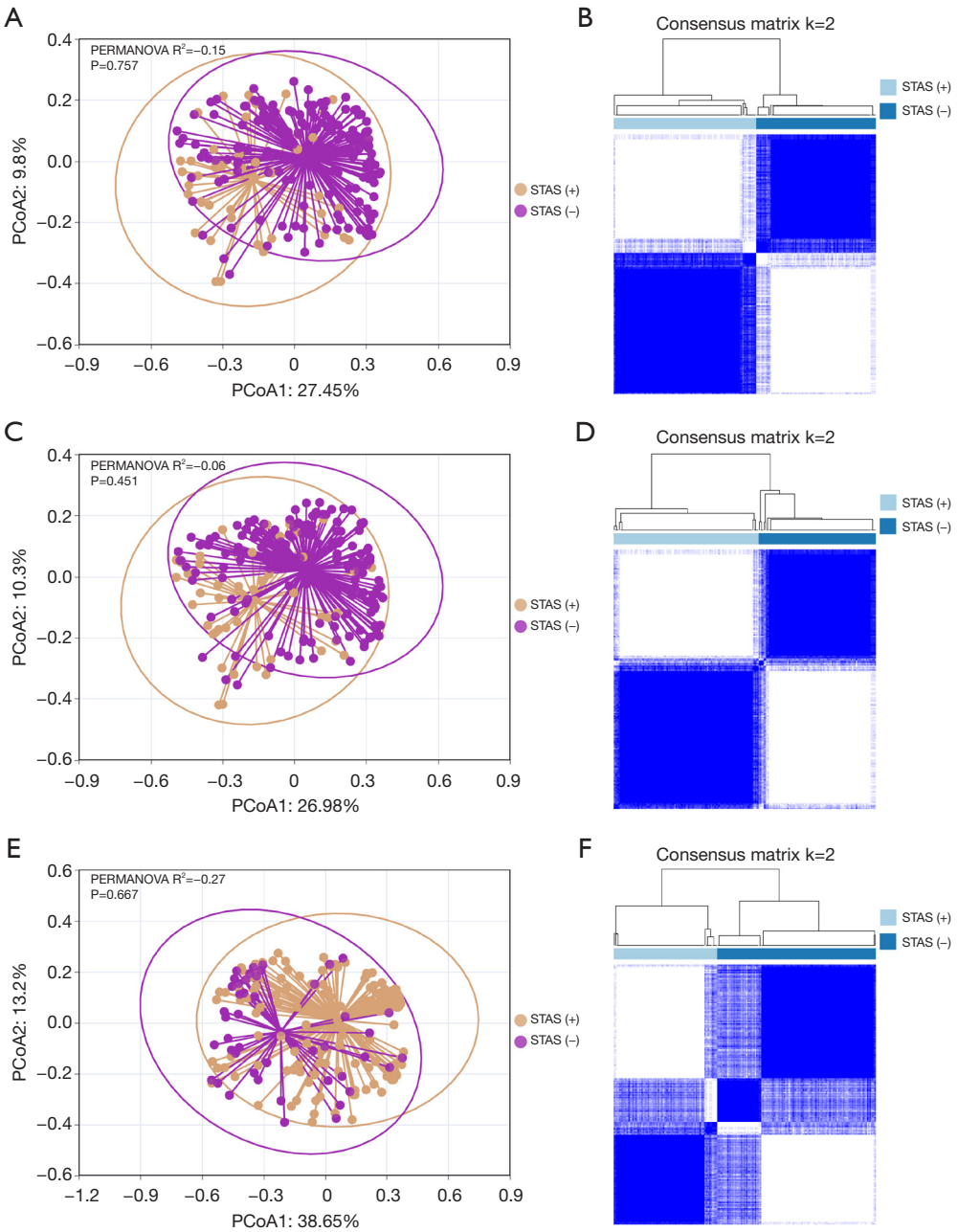

Figure 3 PCA analysis and unsupervised clustering for distinguishing STAS (+) from STAS (–) in peripheral stage I LUAD. (A) PCA scatter plot for intratumoral features with PERMANOVA R^2 statistics, showing the distribution of STAS (+) and STAS (–) samples along the first two principal components. (B) Consensus matrix heatmap for unsupervised clustering at k=2 for intratumoral features, displaying the stability of the two clusters identified among the samples. (C) PCA scatter plot for features from a 3-mm peritumoral expansion, also with PERMANOVA R^2 values, illustrating the variance captured by the principal components and the overlap of STAS groups. (D) Consensus matrix heatmap at k=2 for the 3-mm peritumoral expansion features, indicating the consistency of sample clustering within the identified groups. (E) PCA scatter plot for features from a 5-mm peritumoral expansion, presenting PERMANOVA R^2 statistics to show the explained variance and group distribution. (F) Consensus matrix heatmap at k=2 for the 5-mm peritumoral expansion features, revealing the clustering patterns and potential separation between the STAS (+) and STAS (–) samples. PERMANOVA, permutational multivariate analysis of variance; PCoA, principal coordinates analysis; STAS, tumor spread through air spaces; PCA, principal component analysis; LUAD, lung adenocarcinoma.

Table 4 Summary of 10-fold cross-validation results for 10 machine learning algorithms in the train set of 3 modules

Module	Model name	Recall	Accuracy	F1-score	MCC	AUROC
Intratumoral	SVM_Mean	0.074	0.826	0.187	0.178	0.739
	CatBoost_Mean	0.300	0.829	0.368	0.325	0.724
	RF_Mean	0.334	0.833	0.400	0.346	0.722
	LGBM_Mean	0.352	0.795	0.371	0.261	0.639
	XGB_Mean	0.371	0.816	0.403	0.320	0.685
	GBDT_Mean	0.392	0.769	0.378	0.243	0.622
	DecisionTree_Mean	0.410	0.771	0.387	0.259	0.630
	AdaBoost_Mean	0.413	0.758	0.381	0.237	0.614
	Logistic_Mean	0.584	0.825	0.545	0.452	0.724
	NB_Mean	0.650	0.775	0.509	0.389	0.667
3-mm peritumoral expansion	SVM_Mean	0.074	0.827	0.187	0.188	0.764
	CatBoost_Mean	0.300	0.829	0.368	0.325	0.724
	Logistic_Mean	0.461	0.825	0.545	0.452	0.724
	RF_Mean	0.534	0.833	0.600	0.455	0.722
	XGB_Mean	0.371	0.816	0.403	0.320	0.685
	NB_Mean	0.650	0.775	0.509	0.389	0.667
	LGBM_Mean	0.352	0.795	0.371	0.261	0.639
	DecisionTree_Mean	0.410	0.771	0.387	0.259	0.630
	GBDT_Mean	0.392	0.769	0.378	0.243	0.622
	AdaBoost_Mean	0.413	0.758	0.381	0.237	0.614
5-mm peritumoral expansion	SVM_Mean	0.092	0.829	0.194	0.217	0.801
	CatBoost_Mean	0.351	0.822	0.407	0.329	0.700
	RF_Mean	0.483	0.837	0.589	0.510	0.731
	LGBM_Mean	0.395	0.825	0.441	0.354	0.702
	XGB_Mean	0.524	0.846	0.545	0.468	0.752
	GBDT_Mean	0.469	0.771	0.428	0.299	0.648
	DecisionTree_Mean	0.451	0.771	0.411	0.285	0.641
	AdaBoost_Mean	0.474	0.762	0.419	0.281	0.632
	Logistic_Mean	0.589	0.829	0.540	0.462	0.737
	NB_Mean	0.725	0.736	0.499	0.376	0.653

SVM, Support Vector Machines; CatBoost, Categorical Boosting; RF, Random Forest; LGBM, Light Gradient Boosting Machine; XGB, eXtreme Gradient Boosting; GBDT, Gradient Boosting Decision Tree; AdaBoost, Adaptive Boosting; NB, Naive Bayes; MCC, Matthews correlation coefficient; AUROC, area under the receiver operating characteristic curve.

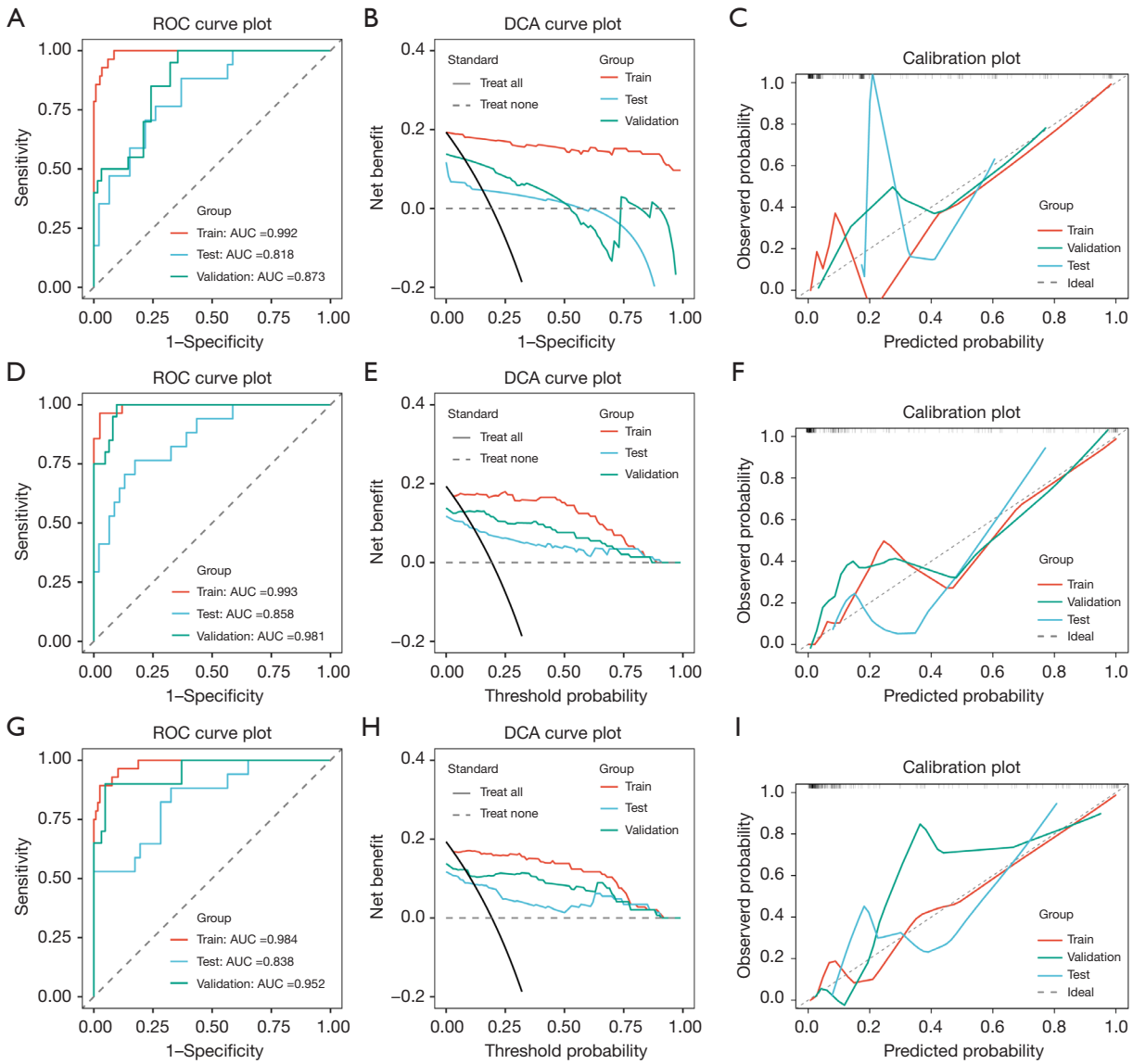

Figure 4 Machine learning model performance for predicting STAS in peripheral stage I LUAD within the tumor and peritumoral expansions. (A) ROC curve plot for the intratumoral model, displaying the model's sensitivity and specificity across different decision thresholds, with AUC scores indicating excellent discrimination for the train, test, and validation sets. (B) DCA plot for the intratumoral model, showing the net benefit across a range of threshold probabilities for the three groups, helping to assess the clinical utility of the model. (C) Calibration plot for the intratumoral model, comparing the predicted probabilities of STAS with the observed outcomes, where the ideal line represents a perfect calibration. (D) ROC curve plot for the 3-mm peritumoral expansion model, with AUC scores suggesting high predictive accuracy, reflected in the curve's proximity to the top left corner. (E) DCA plot for the 3-mm peritumoral expansion model, illustrating net benefits versus a range of threshold probabilities, highlighting the model's potential clinical value. (F) Calibration plot for the 3-mm peritumoral expansion model, demonstrating the calibration of the model in terms of the alignment of predicted probabilities with actual observed frequencies. (G) ROC curve plot for the 5-mm peritumoral expansion model, again showing the AUC scores which denote the model's capability to differentiate between STAS positive and negative cases. (H) DCA plot for the 5-mm peritumoral expansion model, indicating the trade-offs between the benefits of treatment and the risks of unnecessary intervention across different threshold probabilities. (I) Calibration plot for the 5-mm peritumoral expansion model, providing a visual assessment of the prediction accuracy with respect to the ideal calibration curve. ROC, receiver operating characteristic; AUC, area under the curve; DCA, decision curve analyses; STAS, tumor spread through air spaces; LUAD, lung adenocarcinoma.

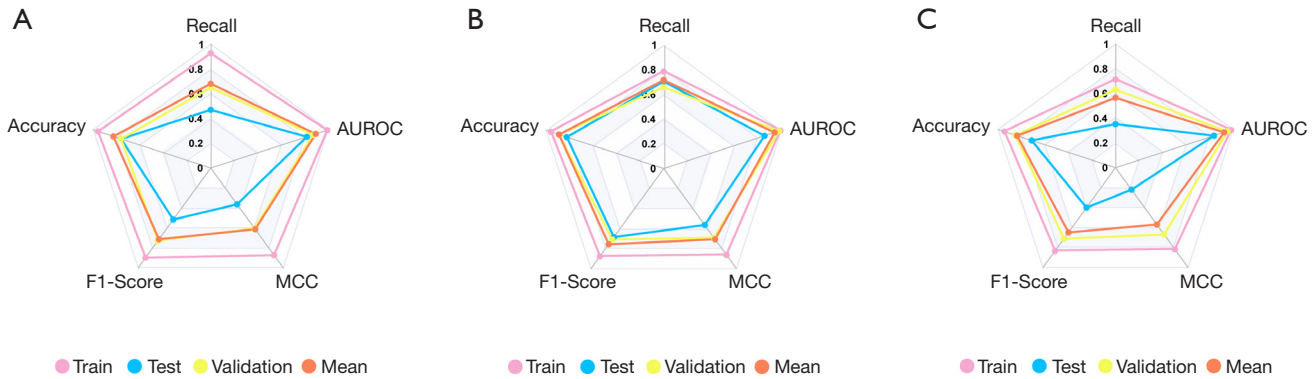

Figure 5 Performance comparison of three different models across train, test, and validation sets using radar charts. (A) Intratumoral model performance metrics. The radar chart illustrates the performance across different metrics including recall, AUROC, MCC, F1-score, and Accuracy. Each line represents the performance in the training (pink), testing (blue), validation (yellow) sets, and their mean (orange). (B) 3-mm peritumoral expansion model performance metrics. Similar to Model 1, this chart shows the evaluation of recall, AUROC, MCC, F1-score, and accuracy for training, testing, validation sets, and the mean values. (C) 5-mm peritumoral expansion model performance metrics. This radar chart demonstrates the performance of the third model on the same metrics (recall, AUROC, MCC, F1-score, accuracy) across the training, testing, validation sets, and their mean values. AUROC, area under the receiver operating characteristic curve; MCC, Matthews Correlation Coefficient.

the feasibility of ML algorithms for preoperative STAS prediction in early-stage lung cancer. Jiang (23) proposed an RF model based on intratumoral radiomics to predict LUAD STAS, achieving an AUC of 0.754 (sensitivity 0.880, specificity 0.588), highlighting the RF algorithm's value in predicting lung cancer STAS and aligning with our current study results. Zhuo's study showed that while peritumoral radiomics models for regions extending 5, 10, and 15 mm from the tumor boundary demonstrated good predictive efficacy, the Hosmer-Lemeshow test indicated poor calibration (24). Currently, there is still debate about the extent of STAS occurrence in peritumoral tissues. Kadota's (7) study identified that STAS most commonly occurs within 1.5–3-mm of the tumor margin. Our results using semi-automatic contouring to extract features from intratumoral plus 3-mm peritumoral and 5-mm peritumoral areas confirmed the added value of models based on intratumoral and peritumoral data, with improved diagnostic performance, particularly at 3-mm from the tumor margin, likely linked to the pathogenesis of STAS. Our models, using semi-automatic segmentation of the entire tumor lesion and peritumoral tissue, performed better than those in studies by Takehana (25) and Liu (26) and were validated in an independent external dataset. Building on this research, our team has developed an online web application that allows users to upload their center's data to validate the feasibility of this model and upload individual patient features to predict the probability of STAS presence.

Limitations

There are several limitations in this study. Firstly, although we included an external validation dataset, further expansion of the data sample size is needed. Secondly, selection bias is an issue in any retrospective study. Additionally, we only included patients with peripheral stage I LUAD, so our conclusions are applicable only to this patient group. Lastly, whether constructing predictive models based solely on peritumoral tissue can improve diagnostic efficacy remains under investigation and will be addressed in future research.

Conclusions

In summary, in peripheral stage I LUAD, preoperative radiological features of the lesions—longest diameter, CTR, spiculation, internal vascular sign, and bronchial anomaly sign—are independent risk factors for the development of STAS. The RF model based on radiomics features of intratumoral and 3-mm peritumoral areas outperforms other ML models in predicting STAS and provides valuable diagnostic information for clinical decision-making.

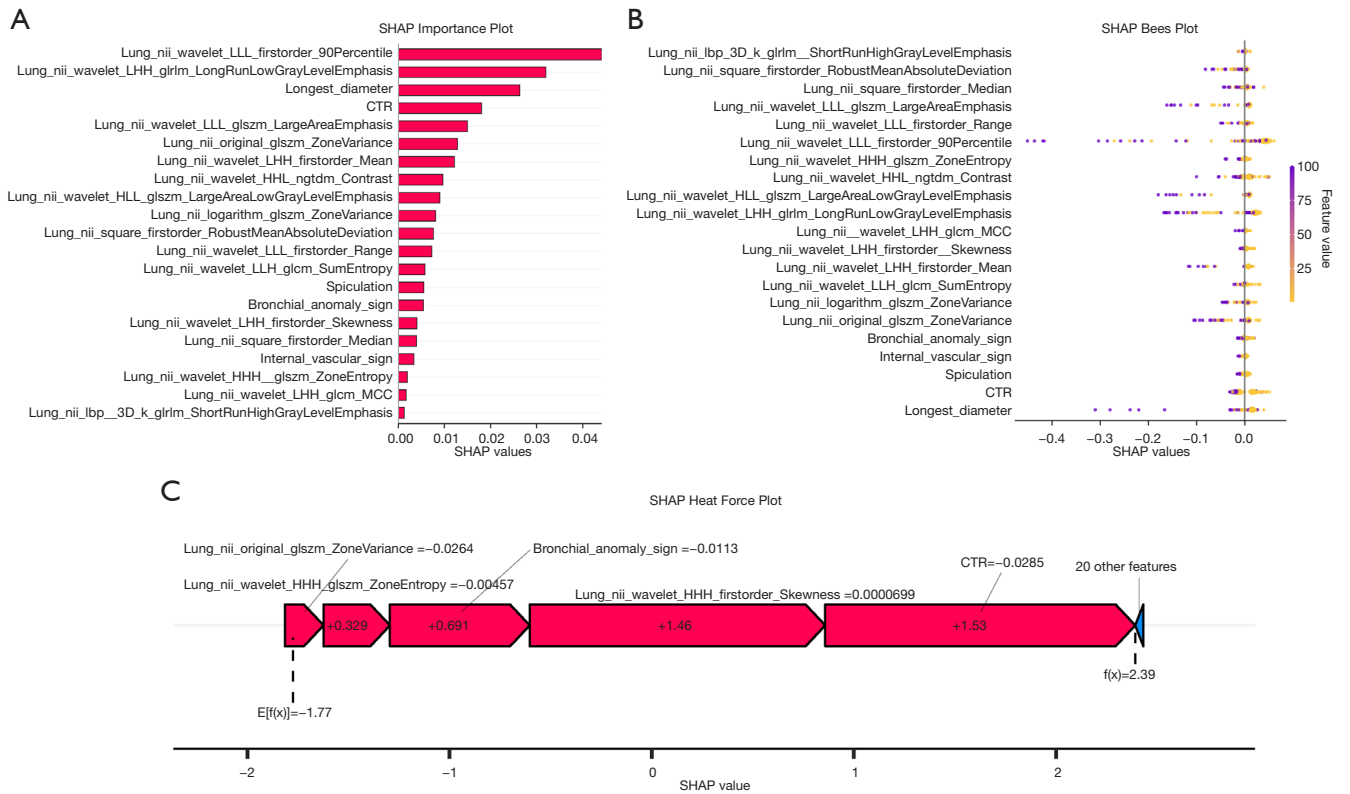

Figure 6 SHAP analysis for a 3-mm peritumoral expansion radiomics features-based predictive model for peripheral stage I LUAD STAS using a random forest algorithm. (A) SHAP importance plot showing the impact of each feature on the model output. The length of each bar represents the magnitude of the feature's importance, with the direction indicating whether the effect is positive or negative with respect to the target outcome. (B) SHAP bees plot illustrating the distribution of the SHAP values for each feature across all samples. Each point represents a sample, with its color denoting the feature value (from low to high), and its position along the x-axis representing the impact on the prediction. (C) SHAP force plot for a single prediction, detailing the contribution of each feature to the final prediction. Features pushing the prediction higher are shown in red, while those with a negative impact are in blue, with the baseline prediction at zero and the final prediction value at the end of the force plot. SHAP, SHapley Additive exPlanations; CTR, consolidation-to-tumor ratio; MCC, Matthews Correlation Coefficient; LLL, low-low-low; LHH, low-high-high; HHL, high-high-low; LLH, low-low-high; HHH, high-high-high; LUAD, lung adenocarcinoma; STAS, tumor spread through air spaces.

Acknowledgments

Funding: This work was supported by Xuzhou Science and Technology Bureau Project (No. KC23229), Clinical Medicine Science and Technology Development Foundation of Jiangsu University, China (No. JLY2021082), and the Natural Science Foundation of China (No. 82001987).

Footnote

Reporting Checklist: The authors have completed the STARD and CLEAR reporting checklists. Available at https://tlcr.amegroups.com/article/view/10.21037/tlcr-24-565/rc

Data Sharing Statement: Available at https://tlcr.amegroups.com/article/view/10.21037/tlcr-24-565/dss

Peer Review File: Available at https://tlcr.amegroups.com/article/view/10.21037/tlcr-24-565/prf

Conflicts of Interest: All authors have completed the ICMJE uniform disclosure form (available at https://tlcr.amegroups.com/article/view/10.21037/tlcr-24-565/coif). The authors have no conflicts of interest to declare.

Ethical Statement: The authors are accountable for all aspects of the work in ensuring that questions related to the accuracy or integrity of any part of the work are appropriately investigated and resolved. The study was conducted in accordance with the Declaration of Helsinki (as revised in 2013). The study was approved by The Xuzhou Hospital Affiliated to Jiangsu University Institutional Review Board (No. 2023-02-027-K01). Written informed consent was exempted due to the retrospective nature.

References

1. Fan L, Wang Y, Zhou Y, et al. Lung Cancer Screening with Low-Dose CT: Baseline Screening Results in Shanghai. Acad Radiol 2019;26:1283-91.
2. Suzuki K, Saji H, Aokage K, et al. Comparison of pulmonary segmentectomy and lobectomy: Safety results of a randomized trial. J Thorac Cardiovasc Surg 2019;158:895-907.
3. Altorki N, Wang X, Kozono D, et al. Lobar or Sublobar Resection for Peripheral Stage IA Non-Small-Cell Lung Cancer. N Engl J Med 2023;388:489-98.
4. Travis WD, Brambilla E, Nicholson AG, et al. The 2015 World Health Organization Classification of Lung Tumors: Impact of Genetic, Clinical and Radiologic Advances Since the 2004 Classification. J Thorac Oncol 2015;10:1243-60.
5. Ren Y, Xie H, Dai C, et al. Prognostic Impact of Tumor Spread Through Air Spaces in Sublobar Resection for 1A Lung Adenocarcinoma Patients. Ann Surg Oncol 2019;26:1901-8.
6. Eguchi T, Kameda K, Lu S, et al. Lobectomy Is Associated with Better Outcomes than Sublobar Resection in Spread through Air Spaces (STAS)-Positive T1 Lung Adenocarcinoma: A Propensity Score-Matched Analysis. J Thorac Oncol 2019;14:87-98.
7. Kadota K, Nitadori JI, Sima CS, et al. Tumor Spread through Air Spaces is an Important Pattern of Invasion and Impacts the Frequency and Location of Recurrences after Limited Resection for Small Stage I Lung Adenocarcinomas. J Thorac Oncol 2015;10:806-14.
8. Chen D, Mao Y, Wen J, et al. Tumor Spread Through Air Spaces in Non-Small Cell Lung Cancer: A Systematic Review and Meta-Analysis. Ann Thorac Surg 2019;108:945-54.
9. Cao H, Zheng Q, Deng C, et al. Prediction of Spread Through Air Spaces (STAS) By Intraoperative Frozen Section for Patients with cT1N0M0 Invasive Lung Adenocarcinoma: A Multi-Center Observational Study (ECTOP-1016). Ann Surg 2024. [Epub ahead of print]. doi: 10.1097/SLA.0000000000006525.
10. Walts AE, Marchevsky AM. Current Evidence Does Not Warrant Frozen Section Evaluation for the Presence of Tumor Spread Through Alveolar Spaces. Arch Pathol Lab Med 2018;142:59-63.
11. Liu C, Wang YF, Wang P, et al. Predictive value of multiple imaging predictive models for spread through air spaces of lung adenocarcinoma: A systematic review and network meta-analysis. Oncol Lett 2024;27:122.
12. Bossuyt PM, Reitsma JB, Bruns DE, et al. STARD 2015: an updated list of essential items for reporting diagnostic accuracy studies. BMJ 2015;351:h5527.
13. Kocak B, Baessler B, Bakas S, et al. CheckList for EvaluAtion of Radiomics research (CLEAR): a step-by-step reporting guideline for authors and reviewers endorsed by ESR and EuSoMII. Insights Imaging 2023;14:75.
14. Amin MB, Edge S, Greene F, et al. AJCC Cancer Staging Manual (8th edition). Springer International Publishing; 2017.
15. Adachi H, Sakamaki K, Nishii T, et al. Lobe-Specific Lymph Node Dissection as a Standard Procedure in Surgery for Non-Small Cell Lung Cancer: A Propensity Score Matching Study. J Thorac Oncol 2017;12:85-93.
16. Garlin-Politis M, Saqi A, Mino-Kenudson M. Spread Through Air Spaces: Interresponder Agreement and Comparison Between Pulmonary and General Pathologists. Mod Pathol 2024;37:100596.
17. Zwanenburg A, Vallières M, Abdalah MA, et al. The Image Biomarker Standardization Initiative: Standardized Quantitative Radiomics for High-Throughput Image-based Phenotyping. Radiology 2020;295:328-38.
18. Travis WD, Eisele M, Nishimura KK, et al. The International Association for the Study of Lung Cancer (IASLC) Staging Project for Lung Cancer: Recommendation to Introduce Spread Through Air

Spaces as a Histologic Descriptor in the Ninth Edition of the TNM Classification of Lung Cancer. Analysis of 4061 Pathologic Stage I NSCLC. J Thorac Oncol 2024;19:1028-51.
19. Qin L, Sun Y, Zhu R, et al. Clinicopathological and CT features of tumor spread through air space in invasive lung adenocarcinoma. Front Oncol 2022;12:959113.
20. Toyokawa G, Yamada Y, Tagawa T, et al. Computed tomography features of resected lung adenocarcinomas with spread through air spaces. J Thorac Cardiovasc Surg 2018;156:1670-1676.e4.
21. Jia C, Jiang HC, Liu C, et al. The correlation between tumor radiological features and spread through air spaces in peripheral stage IA lung adenocarcinoma: a propensity score-matched analysis. J Cardiothorac Surg 2024;19:19.
22. Onozato Y, Nakajima T, Yokota H, et al. Radiomics is feasible for prediction of spread through air spaces in patients with nonsmall cell lung cancer. Sci Rep 2021;11:13526.
23. Jiang C, Luo Y, Yuan J, et al. CT-based radiomics and machine learning to predict spread through air space in lung adenocarcinoma. Eur Radiol 2020;30:4050-7.
24. Zhuo Y, Feng M, Yang S, et al. Radiomics nomograms of tumors and peritumoral regions for the preoperative prediction of spread through air spaces in lung adenocarcinoma. Transl Oncol 2020;13:100820.
25. Takehana K, Sakamoto R, Fujimoto K, et al. Peritumoral radiomics features on preoperative thin-slice CT images can predict the spread through air spaces of lung adenocarcinoma. Sci Rep 2022;12:10323.
26. Liu K, Li K, Wu T, et al. Improving the accuracy of prognosis for clinical stage I solid lung adenocarcinoma by radiomics models covering tumor per se and peritumoral changes on CT. Eur Radiol 2022;32:1065-77.

Cite this article as: Liu C, Meng A, Xue XQ, Wang YF, Jia C, Yao DP, Wu YJ, Huang Q, Gong P, Li XF. Prediction of early lung adenocarcinoma spread through air spaces by machine learning radiomics: a cross-center cohort study. Transl Lung Cancer Res 2024;13(12):3443-3459. doi: 10.21037/tlcr-24-565

